



Multiphase Fe-doped $\text{Ni}_3\text{S}_2/\text{MoO}_x$ electrocatalyst prepared by facile one-step hydrothermal for full-cell water splitting: Effect of Mo on physical and electrochemical properties

Noto Susanto Gultom^a, Chien-Hui Li^{a,b}, Dong-Hau Kuo^{a,b,*}, Mikha Zefanya Silitonga^a

^a Department of Materials Science and Engineering, National Taiwan University of Science and Technology, No.43, Section 4, Keelung Road, Taipei 10607, Taiwan

^b Graduate Institute of Energy and Sustainability Technology, National Taiwan University of Science and Technology, No.43, Section 4, Keelung Road, Taipei 10607, Taiwan

ARTICLE INFO

Keywords:

Bifunctional electrocatalyst

Water splitting

Hydrogen production

Multi-phase

Stack cell electrolyzer

ABSTRACT

Herein, we develop a multiphase strategy to improve the HER performance by incorporating the MoO_x phase with the addition of MoCl_5 during the one-step hydrothermal. Adding MoCl_5 at 0.5 mmol (MFN-0.5) yields the best HER performance, with an overpotential of 261 mV at a current density of 100 mA/cm^2 . The MFN-0.5 catalyst exhibits excellent performance for both HER and OER, enabling it to drive full-cell water splitting with cell potentials of 1.50 and 1.71 V at 10 and 100 mA/cm^2 , respectively. We further scale up the MFN-0.5 ($4 \times 4 \text{ cm}^2$) for a single stack-cell electrolyzer, requiring a cell potential of 1.85 V to achieve a large current density of 250 mA/cm^2 . Incorporating the MoO_x phase accelerates the water dissociation step and protects the metal sulfide surface from oxidation under anodization in an alkaline environment. Our findings offer a promising approach for developing highly efficient catalysts for electrolytic water-splitting applications.

1. Introduction

Electrolytic water splitting, driven by excess renewable energy such as solar panels, has emerged as a promising technique for industrial-scale hydrogen production with a green and sustainable process. Despite its potential, the current data indicates that electrolysis only contributes approximately 4 % of global hydrogen production. In comparison, 96 % still rely on unsustainable and non-green techniques such as steam gas reforming and coal gasification [1]. The main bottleneck of water electrolysis is its high cost, primarily due to the use of a pricey noble metal catalyst such as platinum group material (PGM) and $\text{IrO}_2/\text{RuO}_2$ for hydrogen evolution reaction (HER) and oxygen evolution reaction (OER), respectively [2]. By replacing these expensive metals with cheaper and more active materials, the overall cost of electrolysis can be significantly reduced. Several low-cost electrocatalysts have been developed based on the transition metals and their oxide, sulfide, nitride, and phosphide phases [3–7]. Among these, MoS_2 -based catalysts are considered the most active for HER in acidic conditions [8]. However, the alkaline environment is preferred for practical purposes due to its lower corrosiveness and the absence of costly titanium end plates for

assembling stack cell electrolyzers [9]. Unfortunately, performing the HER half-reaction in an alkaline solution is more challenging than in an acidic condition due to the need for an extra energy barrier in the Volmer step (water dissociation step), which reduces the availability of proton [10]. Therefore, developing an active HER catalyst with low activation energy is an important and urgent task for scientists and engineers.

Heazlewoodite, a nickel sulfide with a Ni_3S_2 phase, appears to be an alternative catalyst for electrocatalytic water splitting in an alkaline environment [11]. However, the pristine Ni_3S_2 has been found to have unsatisfactory activity for both HER and OER. Therefore, engineering modifications are necessary to improve the electrical, physical, chemical, and electrocatalytic properties of Ni_3S_2 . For instance, Kou et al. reported that the pristine Ni_3S_2 required a high overpotential of 240 mV to reach a current density of 10 mA/cm^2 [12]. However, after nitrogen doping, the performance of N-doped Ni_3S_2 significantly improved, with a lower overpotential of 155 mV to reach the same current density. In another study, Tie et al. demonstrated that forming a hybrid $\text{Ti}_3\text{C}_2\text{T}_x/\text{Ni}_3\text{S}_2$ catalyst could significantly enhance HER activity. They found that the overpotential of Ni_3S_2 decreased from 195 mV to 72 mV while the

* Corresponding author at: Department of Materials Science and Engineering, National Taiwan University of Science and Technology, No.43, Section 4, Keelung Road, Taipei 10607, Taiwan.

E-mail address: dhkuo@mail.ntust.edu.tw (D.-H. Kuo).

<https://doi.org/10.1016/j.apcatb.2024.124100>

Received 9 March 2023; Received in revised form 4 October 2023; Accepted 18 April 2024

Available online 19 April 2024

0926-3373/© 2024 Elsevier B.V. All rights reserved.

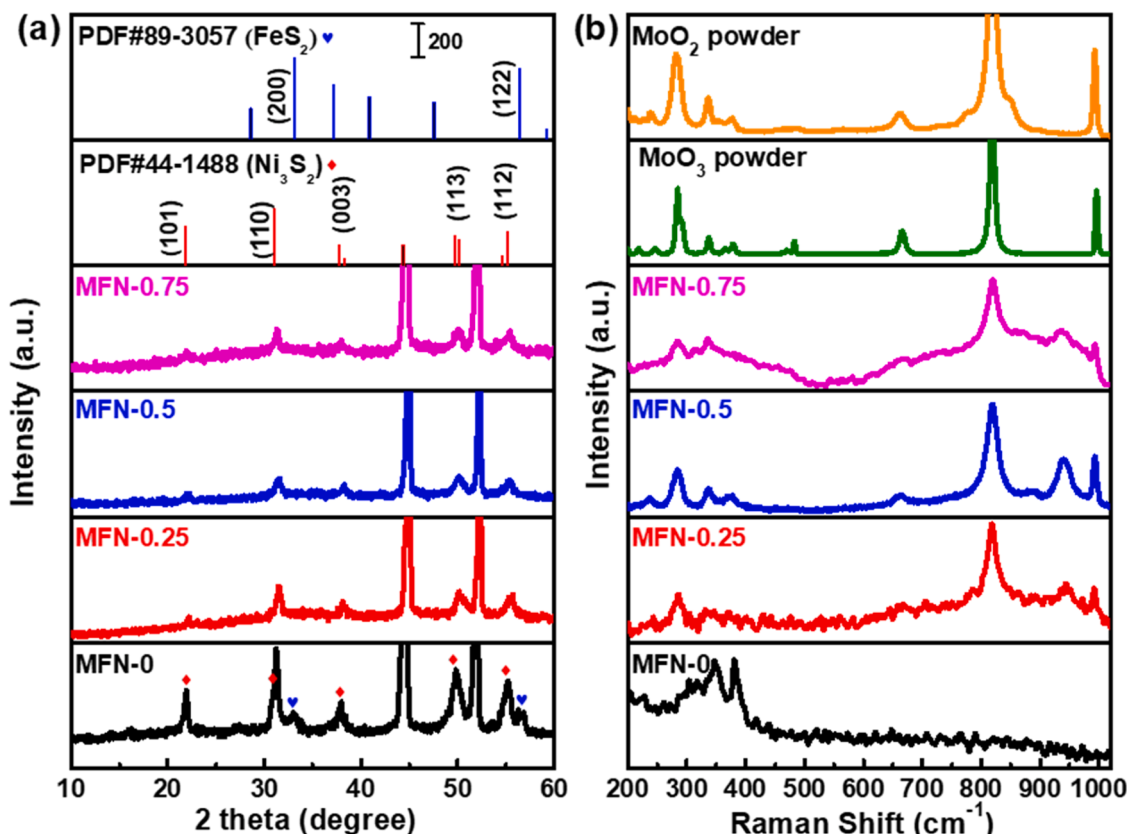


Fig. 1. (a) X-ray diffraction and (b) Raman spectra of MFN-n with different MoCl_5 contents.

Tafel slope reduced from 153 to 45 mV/dec after forming a $\text{Ti}_3\text{C}_2\text{T}_x/\text{-Ni}_3\text{S}_2$ hybrid catalyst [13]. Our early work has shown that adding iron chloride (FeCl_2) during the single-step hydrothermal synthesis significantly improved the OER performance of Ni_3S_2 [14]. The post-characterization revealed that a phase transformation of $\text{Fe-Ni}_3\text{S}_2/\text{FeS}_2$ to NiFe oxyhydroxide occurred and contributed to the excellent OER performance. Unfortunately, the HER activity was unsatisfactory. To activate the catalyst for HER, it is crucial to incorporate another phase that can act as a co-catalyst to cleave the O-H bonding and accelerate the water dissociation [15]. Moreover, using a multiphase electrocatalyst can also improve electron transfer at the surface interface with the electrolyte.

Herein, we aim to improve the HER performance of our previously reported $\text{Fe-Ni}_3\text{S}_2/\text{FeS}_2$ by incorporating amorphous MoO_x through a facile one-step hydrothermal process. Adding MoCl_5 as the MoO_x precursor significantly improves the HER performance. The overpotential of $\text{Fe-doped Ni}_3\text{S}_2/\text{MoO}_x$ with optimal MoCl_5 content (MFN-0.5) catalyst at current densities of 10 and 100 mA/cm^2 are 173 mV and 261 mV, respectively, which is much lower than MoCl_5 -free catalyst. More importantly, the Tafel slope value significantly decreases from 178 to 48 mV/dec, indicating that incorporating amorphous MoO_x can significantly accelerate sluggish HER kinetics. We also demonstrate full-cell water splitting using the bifunctional MFN-0.5 catalyst as both the cathode and anode, achieving lower cell potentials than benchmark catalysts using Pt/C as the cathode and RuO_2 as the anode. Moreover, we scale up the dimension of the MFN-0.5 catalyst to a $4 \times 4 \text{ cm}^2$ single stack cell, which requires a cell potential of 1.85 V at a large current density of 250 mA/cm^2 and is stable during the operation of a 50-hour stability test. The improvement of HER activity is systematically investigated and elucidated based on the evidence from the characterization results.

2. Experimental section

2.1. Chemicals

Cetrimonium bromide (CTAB), thioacetamide (TAA), iron (II) chloride tetrahydrate ($\text{FeCl}_2 \cdot 4 \text{H}_2\text{O}$), and molybdenum chloride (MoCl_5) were purchased from Alfa Aesar. Potassium hydroxide (KOH) was provided by Showa Chemical Industry Co., Ltd.

2.2. Synthesis procedures

Our multiphase $\text{Fe-doped Ni}_3\text{S}_2/\text{MoO}_x$ catalyst was prepared by a facile one-step hydrothermal method, similar to the previous report, with adding extra MoCl_5 at different contents during the synthesis process. A solution containing 1 g of CTAB, 4 mmol of TAA, 0.25 mmol of FeCl_2 , and the appropriate amount of MoCl_5 was dissolved into 100 mL of deionized water under steady stirring. Next, 4 pieces of pre-treated nickel foam (NF) with a $1 \times 1.5 \text{ cm}$ size were immersed in the solution. The hydrothermal synthesis was done in an electric oven at 150 $^\circ\text{C}$ for 12 h. After naturally cooling down to room temperature, those NFs were washed with ethanol and dried in an oven at 70 $^\circ\text{C}$ for 1 h. The resulting catalysts adding 0, 0.25, 0.5, and 0.75 mmol of MoCl_5 were then denoted as MFN-0, MFN-0.25, MFN-0.5, and MFN-0.75, respectively. The catalyst without incorporating FeCl_2 (un-doped $\text{Ni}_3\text{S}_2/\text{MoO}_x$) was also prepared and noted as MN-0.5 for comparison purposes.

2.3. Electrochemical test

All electrochemical tests were performed using a Potentiostat SP-300 (Bi-Logic, France) in the alkaline electrolyte (1 M KOH). A three-electrode system was employed for HER and OER measurements, using Hg/HgO and Pt foil as the reference and counter electrodes, respectively. In contrast, the as-grown catalyst on NF was used as the

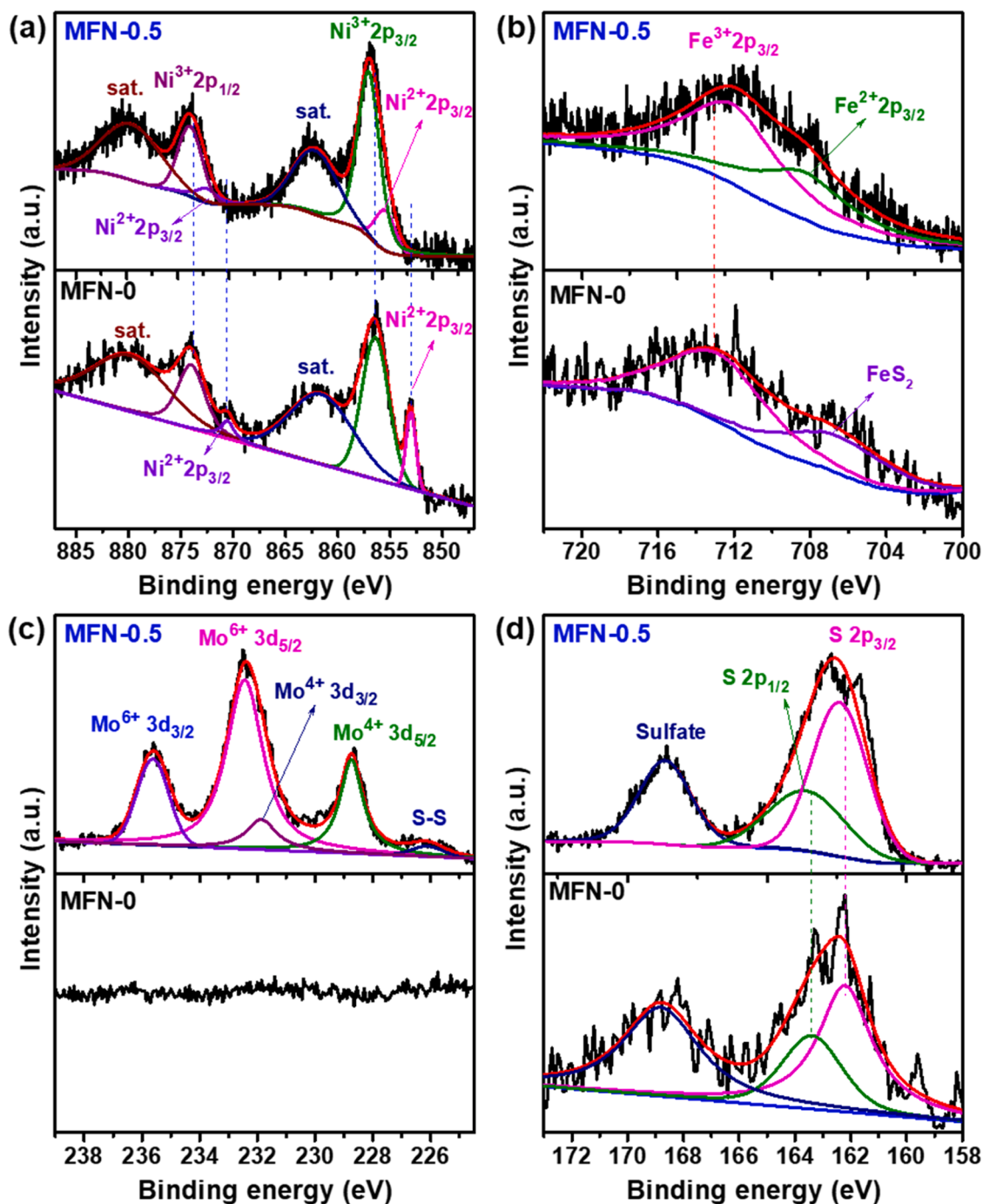


Fig. 2. High-resolution X-ray photoelectron spectroscopy (XPS) analysis (a) Ni 2p, (b) Fe 2p, (c) Mo 3d, and (d) S 2p of MFN-0.5 and MFN-0.

working electrode. The HER and OER performances of the as-prepared catalysts were evaluated using a linear sweep voltammetry (LSV) technique at potential windows of (-0.4) to 0 and 1.2–1.6 V vs. RHE, respectively, with IR compensation of 85 %. The electrochemical impedance spectra (EIS) technique was used at room temperature to investigate the electron transfer resistance behavior. The electrochemical surface active area (ECSA) was determined from the cyclic voltammetry (CV) measurements conducted at different scan rates. A two-electrode system was utilized for the full-cell water-splitting experiments, with the optimal HER and OER catalysts serving as the anode and cathode. To facilitate comparison, a benchmark catalyst using Pt/C and RuO₂ as the HER and OER catalysts, respectively, was also prepared and tested.

2.4. Characterizations

An X-ray diffractometer (D2-PHASER, 2nd generation) was performed under a working voltage of 30 kV to record the X-ray diffraction pattern of the as-synthesized MFN-*n*. Ex-situ Raman spectroscopy (HORIBA iHR550) was utilized to evaluate the molecular structure of the as-synthesized catalysts using a green laser as the excitation energy source. Field-emission scanning electron microscope and transmission electron microscopy were carried out to observe the morphology and nanostructure using JEOL-6500 and JEOL-2100, respectively. X-ray photoelectron spectroscopy (XPS) was performed to probe the surface chemistry using ULVAC-PHI. Inc. / PHI 5000 VersaProbe III with Al K_α. An Electron paramagnetic resonance (EPR-Plus, Bruker) spectrometer

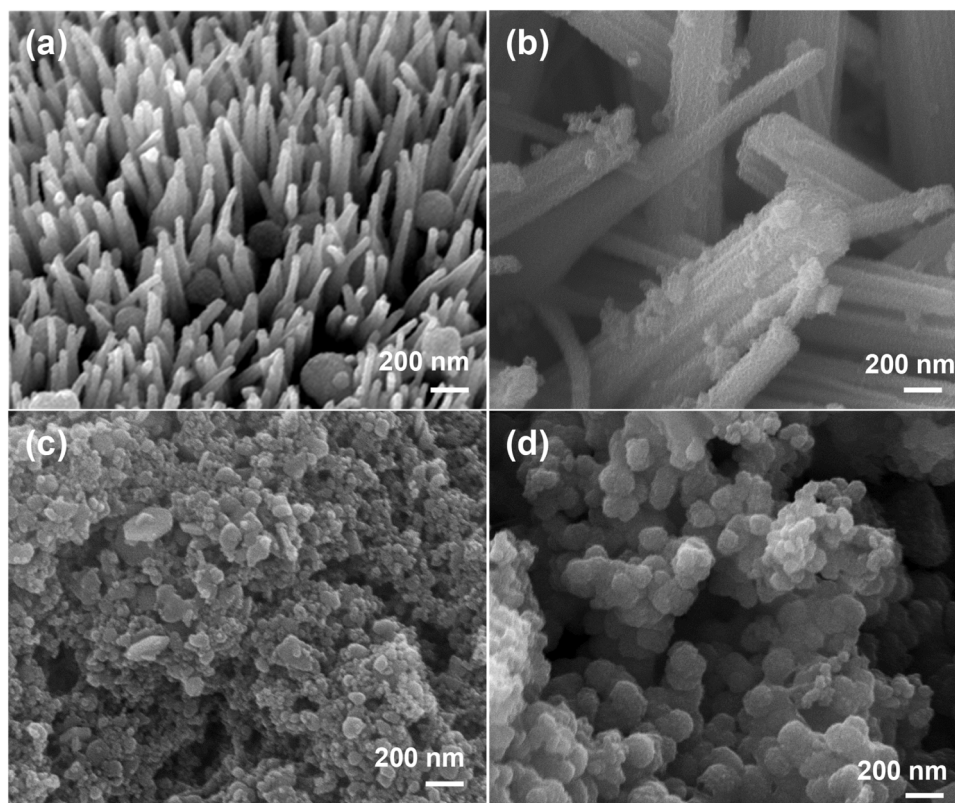


Fig. 3. SEM images of (a) MFN-0, (b) MFN-0.25, (c) MFN-0.5, and (d) MFN-0.75.

with a working frequency of 14.1 GHz was used to confirm the presence of oxygen vacancies.

3. Results and discussion

3.1. Structural analyses

To assess the crystal structural properties of our MFN-*n*, both X-ray diffraction and Raman spectroscopy analyses were performed, with the results shown in Fig. 1. The X-ray diffraction pattern of the catalyst without adding MoCl₅ (MFN-0) indicates the formation of Fe-Ni₃S₂/FeS₂ nanocomposite, as previously reported [14]. After adding different MoCl₅ contents into the hydrothermal synthesis process, all their X-ray diffraction patterns remain similar to that of MoCl₅-free but with reduced intensity, suggesting poorer crystallinity. All peaks were also perfectly matched to the standard JCPDS No. 44–1488 file for the Ni₃S₂ phase with a trigonal crystal structure. Notably, the X-ray diffraction pattern observed no peak corresponding to either the molybdenum sulfide or molybdenum oxide phases. Therefore, Raman analysis was conducted to investigate further the effect of MoCl₅ addition on the structural properties. As depicted in Fig. 1b, the Raman spectra of the catalysts with and without the addition of MoCl₅ were utterly distinct, indicating a change in surface molecular structure. The characteristic Raman peaks of Ni₃S₂ did not appear after adding MoCl₅. We also tested the Raman spectra of commercial MoO₂ and MoO₃ powders for comparison. It can be seen in Fig. 1b that the Raman peaks of MoO₂ and MoO₃ are located at the exact position, such as 288, 336, 376, 662, 821, and 991 cm⁻¹, which are similar to the characteristic peaks of our catalysts with the addition of MoCl₅. The other peak at a wavenumber of 940 cm⁻¹ was related to the Mo-O bonding in the molybdate cluster ion, Mo₇O₂₄⁶⁻ [16]. These results indicate that molybdenum exists as the oxide phase in our catalyst with various oxidation states. Furthermore, molybdenum oxide was amorphous, which the XRD technique could not detect. Therefore, the main reason for poorer crystallinity upon adding

MoCl₅ is that the formation of the MoO_x phase suppresses the crystal growth of the Fe-doped Ni₃S₂, which is further explained in the next section.

3.2. XPS analysis

XPS tool has been regarded as the most powerful technique for characterizing material surface chemistry. The surface chemistry of our MFN-0.5 catalyst was investigated using Al K_α as the energy source, and the results are presented in Fig. 2. The XPS broad spectra in Figure S1a reveal the presence of Ni 2p, Fe 2p, O1s, Mo 3d, and S 2p. The presence of C1s in the broad spectra is well understood in the field because of the carbon contamination and is used for calibration with a value of 284.5 eV. The high-resolution spectrum of Ni 2p demonstrates the presence of multiple peaks, as shown in Fig. 2a. The 854.7 and 872.2 eV binding energies for MFN-0.5 belong to the bivalent Ni²⁺ 2p_{3/2} and Ni²⁺ 2p_{1/2}, respectively [17]. The other peaks at binding energies of 856.3 and 873.8 eV correspond to the spin orbitals of trivalent Ni³⁺ 2p_{3/2} and Ni³⁺ 2p_{1/2}, respectively [18]. The binding energies of the Ni 2p shift to higher energy, especially Ni²⁺ 2p, as compared to that without adding MoCl₅ (MFN-0) owing to the modulation of the electronic structure [19]. Satellite peaks of Ni 2p_{3/2} and Ni 2p_{1/2} can be found at binding energies of 862.1 and 879.7 eV, respectively. Fig. 2b shows the high-resolution XPS spectrum of Fe 2p with a much weaker signal intensity due to its much lower concentration than Ni. With the peak-fitting technique, two peaks can be found at binding energies of 712.1 and 708.3 eV for MNF-0.5, corresponding to the trivalent Fe³⁺ 2p_{3/2} and bivalent Fe²⁺ 2p_{3/2}, respectively [20,21]. The HR-XPS of Fe in the MNF-0 catalyst can be found at a binding energy of 712.8 eV, which is related to the Fe³⁺ 2p_{3/2}. Another peak at a lower energy of 706.5 eV suggests Fe-S bonding in the FeS₂ phase. The high-resolution XPS spectrum of Mo 3d in Fig. 2c exhibits several peaks. The first peak at low energy of 226.1 eV is assigned to the S-S bonding of the S 2s. The appearance of peaks at 232.5 and 235.6 eV confirm the existence of hexavalent Mo⁶⁺ 3d_{5/2} and

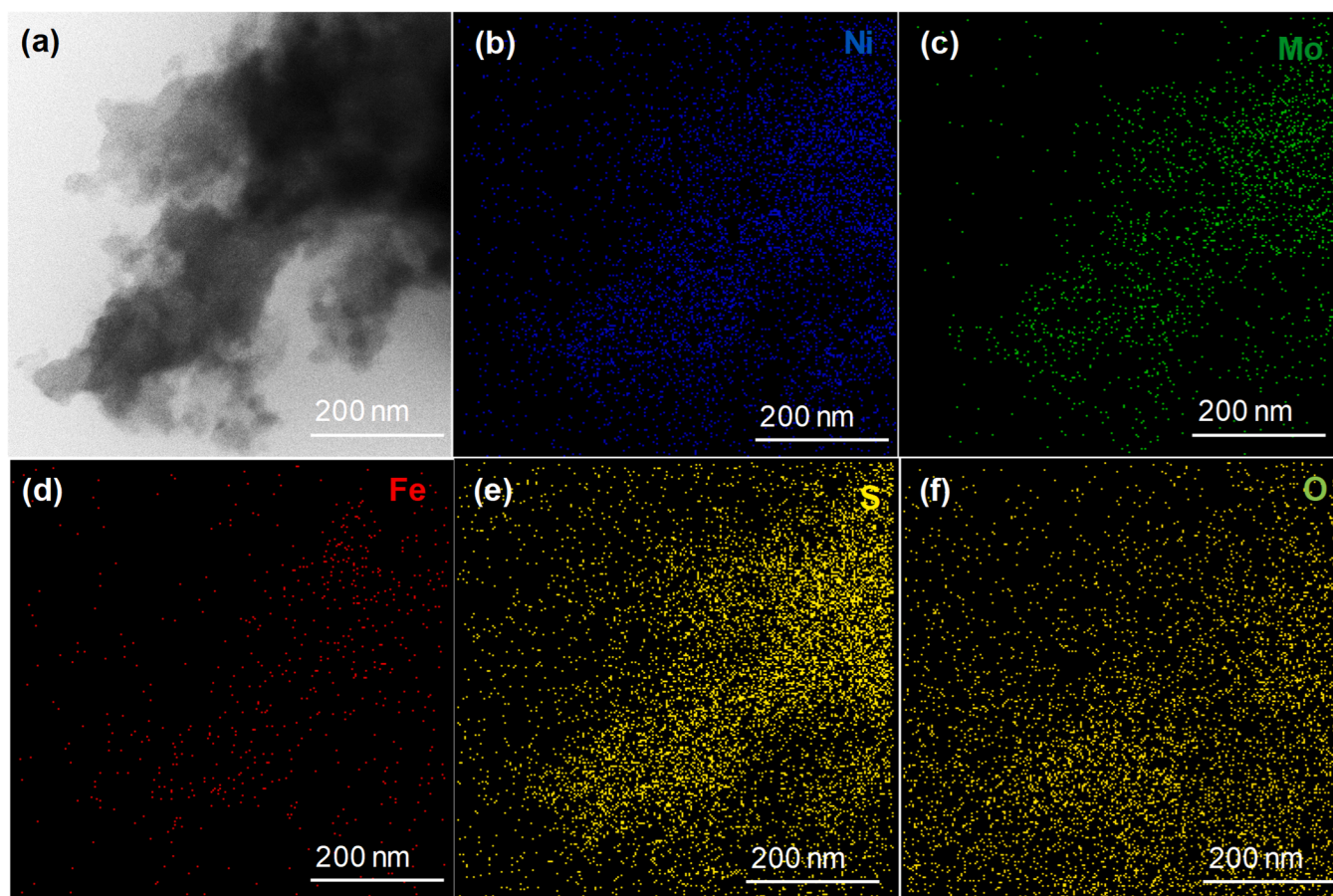


Fig. 4. (a) Transmission electron microscope image of MFN-0.5 and elements mapping of (b) Ni, (c) Mo, (d) Fe, (e) S, and (f) O.

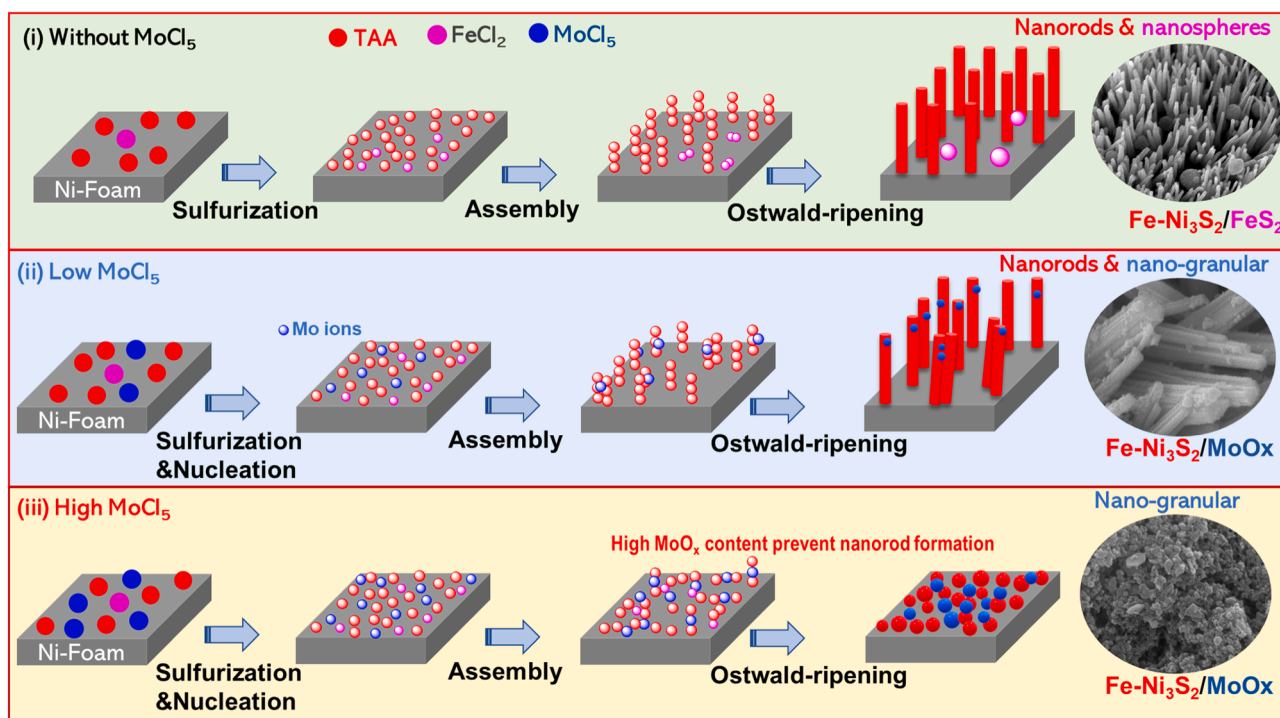
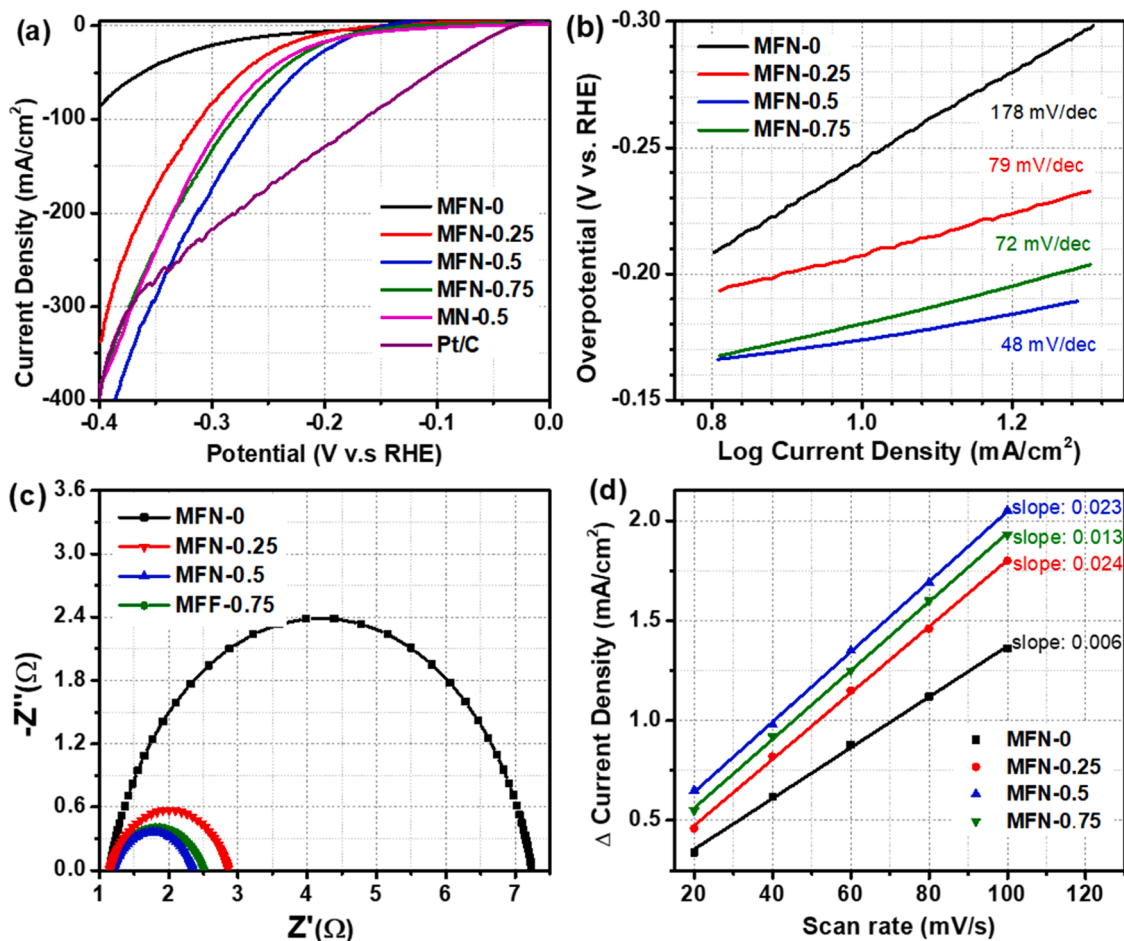
$\text{Mo}^{6+} 3d_{3/2}$, respectively [22]. The other two peaks at 228.8 and 231.9 eV can be assigned as the tetravalent $\text{Mo}^{4+} 3d_{5/2}$ and $\text{Mo}^{4+} 3d_{3/2}$, respectively [23]. This XPS data confirms that our Mo exists with different oxidation states, which is consistent with the Raman analysis in the previous section. Fig. 2d demonstrates the high-resolution XPS spectra of S 2p. Two prominent peaks are observable at binding energies of 162 and 169 eV, corresponding to the metal sulfide and sulfate, respectively [24]. After the deconvolution technique, the S 2p peak can be separated into two peaks at binding energies of 162.4 and 163.6 eV for spin orbitals of $\text{S}^{2-} 2p_{3/2}$ and $\text{S}^{2-} 2p_{1/2}$, respectively [25]. Similar to the binding energies of Ni and Fe, the binding energies of S in the MNF-0.5 sample also shift compared to the binding energies of that MNF-0, suggesting electronic modulation. The high-resolution O1s spectrum in Figure S1b indicates the presence of two peaks at binding energies of 530.7 and 531.7 eV, confirming the oxygen lattices ($\text{O}_{\text{Lat.}}$) and oxygen vacancies ($\text{O}_{\text{Vac.}}$), respectively [26]. Therefore, based on the XRD, Raman, and XPS results, it can be concluded that our catalyst has formed the multiphase of Fe-doped $\text{Ni}_3\text{S}_2/\text{MoO}_x$ after adding MoCl_5 during the synthesis process.

3.3. Microstructure analyses

The effect of adding MoCl_5 on the surface morphology was first analyzed using FE-SEM. Fig. 3a shows the MoCl_5 -free (MFN-0) surface morphology, which consists of nanorods and nanospheres corresponding to the Fe-doped Ni_3S_2 and FeS_2 phases, respectively. Interestingly, upon adding MoCl_5 , the surface morphology is significantly different from that of the MoCl_5 -free specimen, as exhibited in Fig. 3b-c. The formation of tiny spherical shapes is observed on the surface, especially for a higher amount of MoCl_5 . It should be noted that XRD analysis in the

previous section revealed that Ni_3S_2 was the predominant phase. However, SEM analysis clearly did not show the nanorod shape; instead, the formation of porous and aggregate nanoparticles indicates that the morphology of the Ni_3S_2 has changed. The porous structure can facilitate easy water adsorption and gas release during the HER and OER processes. To gain a greater understanding of the nanostructured properties after adding MoCl_5 , TEM analysis was conducted using the MFN-0.5 catalyst. Fig. 4 shows the TEM image of our MFN-0.5, which contains a lot of tiny particles that highly aggregate. Due to the amorphous nature of MoO_x , as revealed by the structural analyses in the previous section and the selected area electron diffraction (SAED) pattern in Figure S2, acquiring a high-quality HR-TEM image was exceedingly challenging during the TEM experiment. The distribution of each element was further evaluated using EDS elemental mapping. Fig. 4b-f demonstrates the uniform distribution of Ni, Fe, Mo, O, and S elements. It is also clear that the contrast of Fe is much lower than those of other elements due to its lower concentration. The element spectra and quantitative analysis of each element are also provided in Figure S3. The atomic percentage of Fe is only 0.72 %, much lower than that of Mo (7.73 %) and Ni (14.11 %).

It is worth highlighting that the formation of the metal sulfide phase of $\text{Fe-Ni}_3\text{S}_2/\text{FeS}_2$ occurred without adding the MoCl_5 precursor. However, even adding a small amount of MoCl_5 has formed a new MoO_x phase, as observed by SEM and Raman analyses. Schematic 1 illustrates the effect of different MoCl_5 contents on phase and morphology. The number of sulfur ions (S^{2-}) was limited during hydrothermal synthesis. Initially, nickel sulfide and iron sulfide phases were formed. The available S^{2-} ion was only sufficient to completely sulfidize the Ni ions from the Ni-foam substrate and the Fe ions from the FeCl_2 precursor for developing the iron-doped metal sulfide (Fe-doped Ni_3S_2) phase. As the

Scheme 1. Illustration of phase and morphology transformation at different MoCl_5 contents.Fig. 5. (a) LSV of HER, (b) Tafel plot derived from the LSV curves, (c) Nyquist plot, and (d) delta current density ($\Delta J = J_a - J_c$) plotted against scan rates of MFN-*n*.

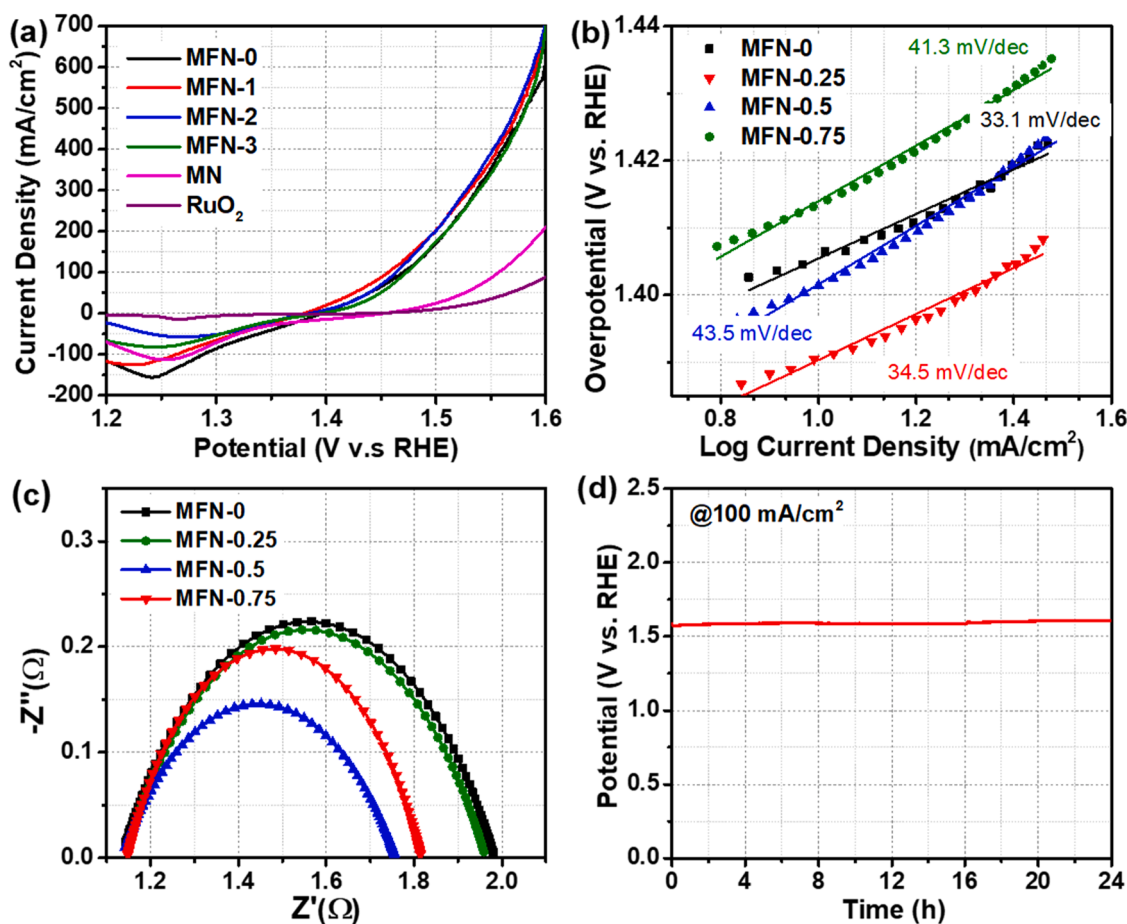


Fig. 6. (a) OER polarization curves, (b) Tafel plot derived from the LSV curves, (c) Nyquist plot of MFN with various MoCl_5 ratios, and (d) OER stability test of MFN-0.5.

amount of the added S^{2-} readily available ion was insufficient to sulfurize the Mo ions upon introducing the extra MoCl_5 precursor, the Mo ions preferred to bond with the oxygen ions from the water to form MoO_x instead of the MoS_x phase. At low MoCl_5 content, the nanorods morphology of Ni_3S_2 is still observable. However, at high MoCl_5 content, in Schematic 1 (iii), the nanorod's morphology was no longer preserved; instead, the formation of tiny nanoparticles that are highly porous and aggregated can be observed. This phenomenon occurs because high Mo ions suppress the crystal growth of Ni_3S_2 and inhibit nanorod formation during the assembly and Ostwald ripening steps. However, it is also important to note that the $\text{Fe-Ni}_3\text{S}_2$ phase continues to exist as the primary phase, even though its morphology has been completely changed to the nano-granular shape due to the high content of the MoO_x phase, as illustrated in Scheme 1.

3.4. Electrocatalytic performance

3.4.1. Hydrogen evolution reaction

As we have reported in our early work, our $\text{Fe-Ni}_3\text{S}_2/\text{FeS}_2$ nanocomposite had excellent OER performance but poor HER performance. This study aims to improve its HER activity by adding MoCl_5 during the facile one-step hydrothermal synthesis. Fig. 5a compares the HER performance of MFN-*n* with different MoCl_5 contents. Our MFN-0 without adding MoCl_5 has poor HER activity, as demonstrated in Fig. 5a. The overpotential to reach a low current density of 10 mA/cm^2 was 243 mV. In addition, it could not achieve a large current density ($>100 \text{ mA/cm}^2$) at the same potential as other catalysts. Interestingly, by adding only a small amount of 0.25 mmol MoCl_5 in the MFN-0.25 catalyst, its HER performance was greatly enhanced as compared to that of MFN-0. Its

overpotentials at current densities of 10 and 100 mA/cm^2 were 207 and 311 mV, respectively. As the amount of MoCl_5 was increased to 0.5 mmol (MFN-0.5), the highest HER performance was achieved, indicating the optimal MoCl_5 content. The overpotentials of the MFN-0.5 catalyst at current densities of 10 and 100 mA/cm^2 were 173 and 261 mV, respectively. Moreover, the maximum current density of the MFN-0.5 catalyst was almost four times higher than that of the MoCl_5 -free catalyst. However, further increasing the MoCl_5 amount resulted in a degradation of the HER performance, although it was still much better than that of the MoCl_5 -free catalyst. Un-doped $\text{Ni}_3\text{S}_2/\text{MoO}_x$ (MN-0.5) shows lower HER activity than our MFN-0.5 catalyst, but it performs better than MFN-0, indicating that the presence of Mo ions is more responsible for the improvement of HER. Furthermore, the HER benchmark catalyst Pt/C is also compared in Fig. 5a. At a low current density ($<100 \text{ mA/cm}^2$), the Pt/C outperforms our MFN-0.5 catalyst. However, at relatively high current density, their performance is comparable. The derived Tafel value from the LSV data is critical in evaluating the reaction kinetics. Then, the Tafel value of MFN-*n* was computed according to previous work and plotted in Fig. 5b [27]. Without the addition of MoCl_5 , the MFN-0 catalyst exhibited a high Tafel slope of 178 mV/dec, indicating very sluggish HER kinetics. The Tafel slope value significantly decreased to 79 mV/dec after adding 0.25 mmol of MoCl_5 . The Tafel slope value was further reduced to 48 mV/dec with the optimal condition in the MFN-0.5 catalyst. The MFN-0.75 catalyst had a Tafel slope value of 72 mV/dec and was much lower than that of the MFN-0 catalyst. This data suggests incorporating MoO_x in the $\text{Fe-Ni}_3\text{S}_2$ system boosts the HER kinetics.

Next, we investigate the electron transfer behavior during the HER with the EIS technique by applying an extra potential of -300 mV .

Table 1Summary of electrocatalytic HER performance of MFN-*n*.

Catalyst	Overpotentials (mV vs. RHE)		Tafel slopes (mV/dec)	R_{ct} (Ω)	ECSA (cm^2)	TOF at the potential of -0.3 V
	10 mA/ cm^{-2}	100 mA/ cm^{-2}				
MFN-0	243	-	178	6.09	317	0.18
MFN-0.25	207	311	79	1.71	415	0.57
MFN-0.5	173	261	48	1.18	442	1.15
MFN-0.75	181	281	72	1.36	427	0.89

Fig. 5c shows the Nyquist plot of MFN-*n* after fitting to a Randle circuit model. The charge transfer resistance (R_{ct}) values, which were proportional to the diameter of semicircles, were determined to be 6.1, 1.7, 1.1, and 1.4 ohms for MFN-0, MFN-0.25, MFN-0.5, and MFN-0.75, respectively. This result indicates that our MFN-0.5 catalyst has the lowest resistance to facilitate easy electron transport between catalyst and electrolyte. Moreover, this data is consistent with the Tafel slope and LSV analyses. Electrocatalytic surface active area (ECSA), another critical factor in determining electrocatalytic activity, was also estimated based on the CV measurements at various scan rates (Figure S4). Fig. 6d demonstrates the plot of delta current density (ΔJ) against the scan rates to obtain the double-layer capacitance (C_{dl}). The C_{dl} value is equal to the slope value of the linear fit of the plot in Fig. 6d. Hence, the C_{dl} values of MFN-0, MFN-0.25, MFN-0.5, and MFN-0.75 were 12.7, 16.6, 17.7, and

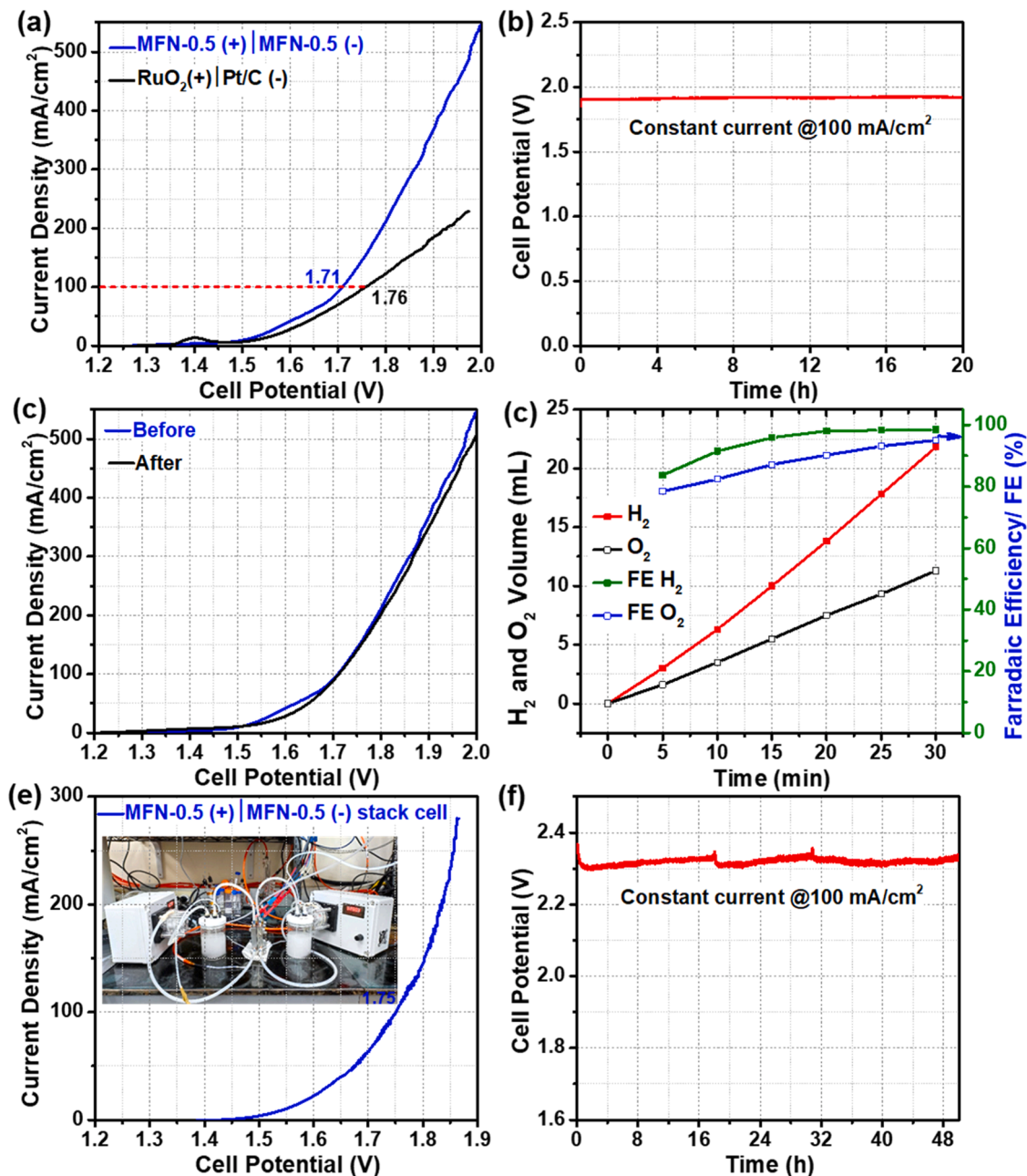


Fig. 7. (a) LSV of full-cell water splitting of MFN-0.5(+) || MFN-0.5 (-) and RuO₂(+) || Pt/C (-) with a two-electrode system, (b) the stability test with chronopotentiometry technique at a current density of 100 mA/cm², (c) LSV before and after stability test, (d) the hydrogen and oxygen production and faradaic efficiencies of MFN-0.5, (e) the LSV of full-cell water splitting using MFN-0.5 catalyst with a single stack cell design of 4 × 4 cm², and (f) the stability test of the MFN-0.5 stack cell.

17.1 mF/cm², respectively. Then, the actual ECSA number could be obtained by dividing the C_{dl} value by the standard capacitance (C_s) of 40 μ F/cm² per cm²_{ECSA} [28]. Therefore, the actual surface active numbers were 317, 415, 442, and 427 per cm²_{ECSA} for MFN-0, MFN-0.25, MFN-0.5, and MFN-0.75, respectively. The ECSA value increased only about 39 % after adding 0.5 mmol of MoCl₅, demonstrating that ECSA is not the primary factor in enhancing the HER performance. To further investigate the intrinsic activity after the addition of MoCl₅, the turnover frequency (TOF) values were additionally calculated. The TOF value of MFN-0.5 was 1.15 H₂/s, which was higher than those of MFN-0 (0.18 H₂/s), MFN-0.25 (0.57 H₂/s), and MFN-0.75 (0.89 H₂/s). The TOF value of MFN-0.5 was the highest among the as-synthesized MFN-*n*, indicating the best intrinsic activity after incorporating MoO_x. More importantly, the LSV normalized to the ECSA (Figure S5) shows the inherent activity enhancement. The electrocatalytic HER properties of the as-synthesized MFN-*n* are listed in Table 1. Furthermore, HER stability was evaluated using a chronopotentiometry technique. Figure S6 depicts the required potential to drive a current density of 100 mA/cm², which almost remains constant, suggesting stable performance.

3.4.2. Oxygen evolution reaction

We also evaluated the effect of the addition of MoCl₅ on OER performance, as shown in Fig. 6a. It is evident that adding MoCl₅ only slightly improves the OER performance. The overpotential of MFN-0.5 at current densities of 100 and 500 mA/cm² were 233 and 341 mV, which was similar to those of MFN-0 (239 and 350 mV), MFN-0.25 (226 and 345 mV), and MFN-0.75 (239 and 351 mV) at the same current densities. The OER performance of the catalyst without adding FeCl₂ (MN-0.5) shows poor OER activity, suggesting that incorporating the Fe ions is responsible for the high OER performance. RuO₂, the OER benchmark catalyst, was tested and compared in Fig. 6a. It is much less active than all Fe-doped Ni₃S₂/MoO_x catalysts and comparable to MN-0.5. Fig. 6b demonstrates the calculated Tafel slope based on the OER LSV curves. It is clear that the Tafel value did not significantly change, indicating there is no effect on OER kinetics. The electron transfer during the OER was also evaluated with the EIS technique. As shown in Fig. 6c, the diameter of a semicircle in the Nyquist plot is similar at various MoCl₅ ratios, indicating a similar charge transfer resistance. Then, the actual charge transfer resistance was estimated after fitting to an equivalent circuit to be 0.85, 0.66, 0.62, and 0.82 ohm for MFN-0, MFN-0.25, MFN-0.5, and MFN-0.75, respectively. The OER stability of the MFN-0.5 was tested at a current density of 100 mA/cm², as shown in Fig. 6d. There is no change in the potential to reach that current density even after 24 hours, demonstrating the excellent OER stability of our catalyst.

3.4.3. Full-cell water splitting

Inspired by the excellent performance of our catalyst for both HER and OER, we further evaluate the performance of our MFN-0.5 as the best HER and OER catalyst to drive full-cell water splitting with a two-electrode system at room temperature. The LSV curve in Fig. 7a demonstrates an excellent performance of our bifunctional MFN-0.5(+)||MFN-0.5(-) catalyst, with a cell potential of 1.71 V to reach a large current density of 100 mA/cm². For comparison, the benchmark catalyst RuO₂(+)||Pt/C(-) was prepared and tested to drive full-cell water splitting under the same conditions as the MFN-0.5 catalyst. Its cell potential to reach a 100 mA/cm² current density was 1.76 V, slightly higher than the bifunctional MFN-0.5 catalyst. At a higher potential of 1.95 V, our catalyst can reach a large current density of 450 mA/cm², while those RuO₂(+)||Pt/C(-) can only reach 217 mA/cm². Hence, it is evident that our catalyst outperforms those benchmark catalysts. In addition, as stability is an important parameter for practical application, we evaluated our catalyst's stability using a continuous constant current density of 100 mA/cm². Fig. 7b shows the stability test of the bifunctional MFN-0.5 catalyst for a duration of 20 hours with a negligible potential increment. Moreover, the LSV curve before and after the

Table 2

Comparison of the cell potential of this report with several bifunctional Ni₃S₂-based electrocatalysts.

No.	Catalysts	Cell voltage (V) @100 mA/cm ²	Year	Ref.
1	MFN-0.5 (Fe-doped Ni ₃ S ₂ /MoO _x)	1.71		This report
2	Ni ₃ S ₂	2.0	2019	[30]
3	Ni ₃ S ₂ -MoS _x /NF composite	1.9	2019	[31]
4	Co ₉ S ₈ -Ni ₃ S ₂ -CNTs	2.25	2019	[32]
5	MoS ₂ /Co ₉ S ₈ /Ni ₃ S ₂	2.0	2019	[33]
6	Ni ₃ S ₂ -MoS ₂ -Ni ₃ S ₂ @Ni foam	1.82	2020	[34]
7	Ni ₃ S ₂ @Ni ₃ B	1.90	2021	[35]
8	Mo-Ni ₃ S ₈ /Ni ₃ S ₂	1.79	2021	[36]
9	MoS ₂ /NiS ₂ /CC-2	1.8	2021	[37]
10	Co ₃ O ₄ @Mo-Co ₃ S ₄ -Ni ₃ S ₂	2.05	2022	[38]
11	Ni ₃ S ₂ /FeNi ₂ S ₄	1.86	2022	[39]
12	Co/MoO ₂ @N-doped carbon	1.75	2022	[40]
13	VS ₄ /Ni ₃ S ₂	1.85	2022	[41]
14	Ni ₃ (BO ₃) ₂ -Ni ₃ S ₂	1.99	2022	[42]
15	Ni ₃ S ₂ /Co ₉ S ₈	1.84	2023	[43]
16	Li, V co-doped Ni ₃ S ₂	1.70	2023	[44]
17	Ni ₃ S ₂ /NiMo ₂ S ₄ -POM/NF	1.94	2023	[45]
18	Ni-Fe-Mo sulfide	1.68	2022	[46]
19	N-Co ₉ S ₈ /Ni ₃ S ₂	1.79	2023	[47]
20	CoS ₂ @N-doped carbon	1.75	2023	[48]
21	ZnCoNiS	1.85	2023	[49]
22	NiMo ₃ S ₄	1.68	2023	[49]
23	(NiFeCoV) ₂ S ₂	1.69	2023	[50]
24	P-O doped CoS	1.80	2023	[51]
25	NiAu-MoS ₂	1.74	2023	[52]

stability test was also recorded. As demonstrated in Fig. 7c, the LSV curves coincide, indicating an excellent stability performance of our bifunctional MFN-0.5 catalyst. The actual generated amounts of H₂ and O₂ gases were measured by a water-displacement technique, as shown in Fig. 7d. Our bifunctional MFN-0.5 catalyst could generate 59.9 and 27.4 mL of hydrogen and oxygen under a constant current density of 100 mA/cm² for 30 minutes, respectively. To evaluate the energy conversion efficiency of overall water splitting using our MFN-0.5 catalyst, Faradaic efficiency was calculated and presented in Fig. 7d. Faradaic efficiencies for H₂ and O₂ are close to 100 %, indicating a good energy conversion efficiency. To further evaluate the performance of the bifunctional MFN-0.5 catalyst for practical application, a single-stack cell was assembled (inset Fig. 7f) and tested according to our recent report [29]. The dimension of the MFN-0.5 catalyst was scaled up to 4 × 4 cm² for this purpose. Fig. 7e shows the LSV curve of the bifunctional MFN-0.5 with a single stack cell in 1 M KOH at room temperature. Based on that data, the cell potentials to achieve large current densities of 100 and 250 mA/cm² were 1.75 and 1.85 V, respectively. Then, the stability of the stack cell electrolyzer was evaluated with a constant current density of 250 mA/cm². As demonstrated in Fig. 7f, the required potential almost did not change, indicating a stable performance during the stability test of 50 hours.

Table 2 compares the performance of our bifunctional MFN-0.5 catalyst with some reported bifunctional electrocatalysts at a large current density of 100 mA/cm². With a cell potential of 1.71 V at 100 mA/cm², our present Fe-doped Ni₃S₂/MoO_x catalyst was better than other metal sulfide and Ni₃S₂-based catalysts, such as P-O doped CoS (1.8 V), NiAu-MoS₂Ni₃S₂-MoS_x (1.74 V), CoS₂@N-doped carbon (1.75 V), Ni₃S₂-MoS_x (1.9 V), Ni₃S₂-MoS₂-Ni₃S₂ (1.82 V), Co₉S₈-Ni₃S₂-CNTs (2.25 V), MoS₂/Co₉S₈/Ni₃S₂ (2.0 V), and Co₃O₄@Mo-Co₃S₄-Ni₃S₂ (2.05 V).

3.5. Electrocatalytic enhancement and mechanism

According to the previous Raman analysis findings, adding MoCl₅ during the one-step hydrothermal synthesis resulted in a new

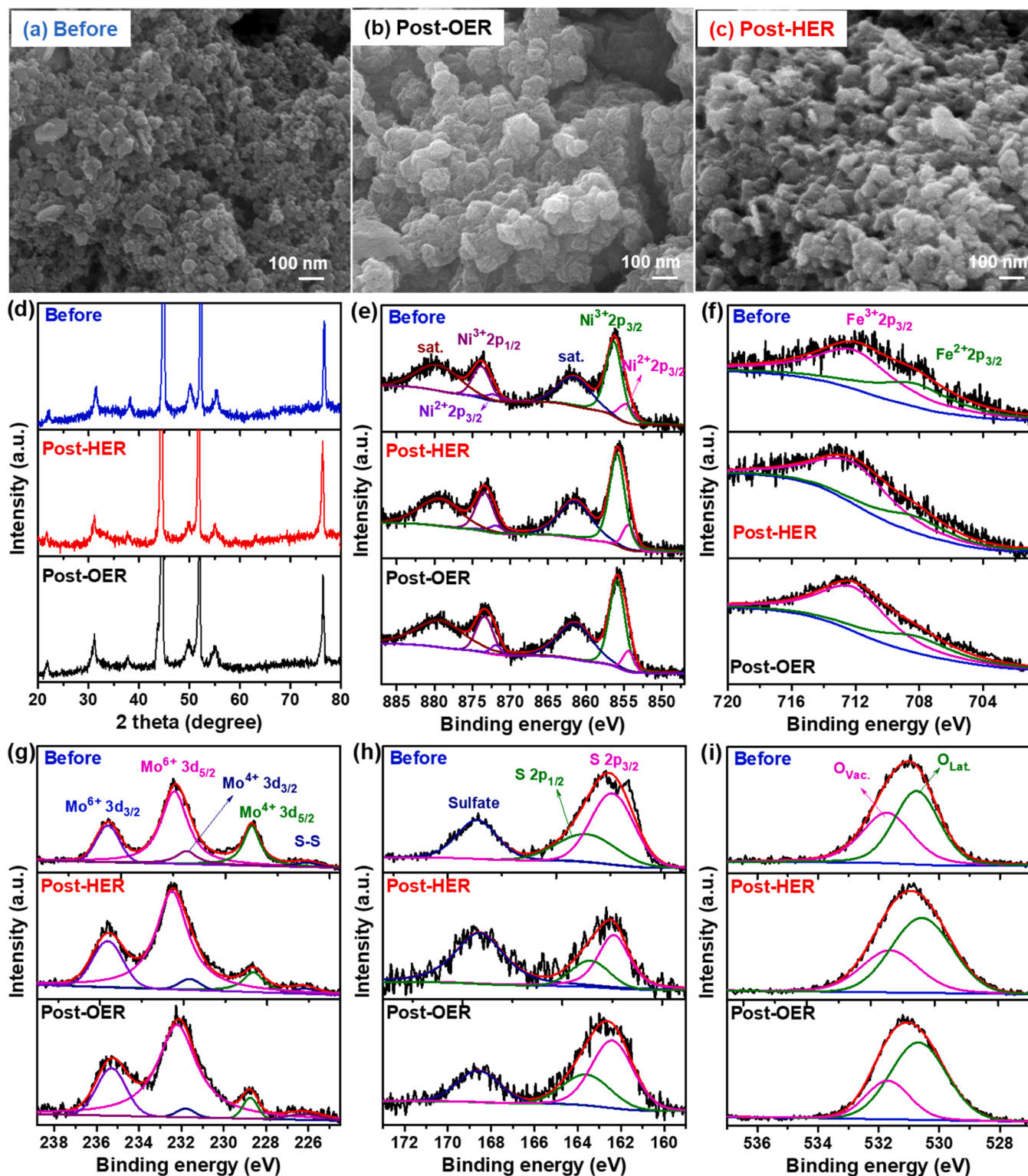
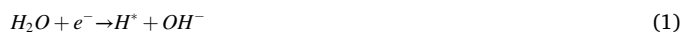


Fig. 8. Post characterization analyses. (a, b, c) SEM images, (d) XRD pattern, and High-resolution XPS spectrum for (e) Ni, (f) Fe, (g) Mo, (h) S, and (i) O of the MNF-0.5 before and after being used for water splitting.

amorphous phase of MoO_x . This new phase has promoted a notable enhancement in the HER performance, as proved by the LSV curve in Fig. 5a. After the incorporation of MoO_x , the Tafel slope value has dropped significantly, from 178 to 48 mV/dec. This finding indicates that there is a considerable acceleration during the HER. In addition, that Tafel slope value also provides the pathway of hydrogen generation, which is the Volmer-Heyrovsky step, as demonstrated in Eqs. (1) and (2)

[53].



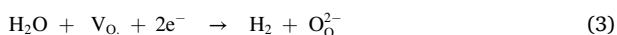
Our catalyst has demonstrated a significant enhancement in HER activity, which can be attributed to the following reasons:

i. The surface structure morphology

The surface morphology of our bifunctional MFN-0.5 catalyst comprises nanoparticles that are extremely small and have abundant pores. This characteristic is advantageous not only for the surface interface with the electrolyte but also for gas release. Due to their nanoscale size, these particles have a more active surface area easily accessible for carrying out the HER reactions.

ii. The extra phase of MoO_x

The Tafel slope data suggests that MoO_x as the second phase has been shown to play a significant role in accelerating the HER reaction. This MoO_x, with the presence of oxygen vacancies, aids in the water dissociation stage by cleaving the strong O-H bonds of the water, ultimately providing additional protons that can be reduced into hydrogen gas, as summarized in Eq. (3). The EPR analysis in Figure S7 clearly shows much higher peak intensity for MFN-0.5 than MFN-0 at a magnetic field of about 3350 G corresponding to the g-value of 2.007. According to the literature, that value indicates the presence of oxygen vacancies [54]. Therefore, it is concluded that oxygen vacancies of the MoO_x phase are the active side for HER. The control sample MFN-0 without oxygen vacancies has much lower HER performance.

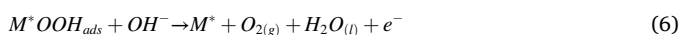
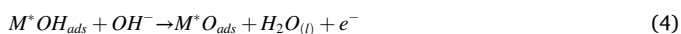


iii. Electron transport

Upon the addition of the optimal concentration of the MoCl₅, there was a significant increase in the improvement of the electron transfer resistance. The value of the electron transfer resistance significantly declined from 6.09 ohm down to 1.18 ohm, as is evident in Fig. 5c. The MoO_x phase facilitates more accessible electron transport from the electrolyte to the catalyst.

Overall, the enhanced HER activity of our catalyst can be attributed to its unique surface structure morphology, the presence of MoO_x as a secondary phase, and improved electron transport. These findings highlight the potential of our strategy to activate the HER catalyst for industrial applications in catalysis and renewable energy.

The mechanism of oxygen generation also can be predicted based on Tafel value derived from the LSV of OER, as simplified in Eqs. (3)–(6) [55].



3.6. Post-characterization

Our bifunctional MFN-0.5 catalyst, after being used to perform full-cell water splitting, was systematically characterized to further evaluate the stability of its physicochemical properties. Fig. 8a-c exhibit that the surface morphology of the bifunctional MFN-0.5 catalyst was not significantly different before, post-HER, and post-OER, indicating no change in morphology. As shown in Figure S8, the EDS mapping also depicts the uniform distribution of each element. Furthermore, XRD analysis in Fig. 8d also verifies the similar X-ray diffraction pattern before, post-HER, and post-OER, which further confirms the outstanding phase stability of our bifunctional MFN-0.5 catalyst. XPS analyses depicted in Fig. 8e-i exhibit a similar high-resolution spectrum before, post-HER, and post-OER, indicating the absence of cation and anion changes during the reduction and oxidation reactions. It should be highlighted that without the presence of the MoO_x phase, a phase transformation of the metal sulfide to the metal oxyhydroxide was

confirmed after the OER test in our early report [14]. In contrast, the MFN-0.5 catalyst with the extra MoO_x phase did not undergo any phase transformation after being used as the anode to execute the OER. Therefore, the MoO_x phase can protect and make the surface much more stable under the applied positive potential in a strong alkaline environment.

4. Conclusions

We have successfully developed a facile one-step hydrothermal synthesis method to prepare a multiphase Fe-doped Ni₃S₂/MoO_x electrocatalyst. The addition of MoCl₅ significantly affected the surface morphology from the nanorods to the highly porous and aggregate nanoparticles and greatly enhanced the HER performance. The bifunctional MFN-0.5 catalyst with an optimal MoCl₅ content of 0.5 mmol performed the best activity for both HER and OER. The significant improvement of HER activity was attributed to the presence of the MoO_x phase as an accelerator in the water dissociation step via oxygen vacancy trapping. The bifunctional MFN-0.5 catalyst could drive full-cell water splitting with a cell potential of 1.71 V at a current density of 100 mA/cm², outperforming the benchmark catalyst of RuO₂(+)|Pt/C (-). The scale-up of a 4 × 4 cm² MNF-0.5 single-stack cell electrolyzer with a cell potential of 1.85 V at a large current density of 250 mA/cm² and good stability performance demonstrated the potential of our catalyst for practical application. This work provides a promising strategy for transforming the OER catalyst into an active HER catalyst and driving full-cell water splitting in an alkaline solution by forming a multiphase electrocatalyst.

Declaration of Competing Interest

The authors declare that they have no known competing financial interests or personal relationships that could have appeared to influence the work reported in this paper.

Data availability

Data will be made available on request.

Acknowledgments

This work was supported by the National Science and Technology Council (NSTC) of Taiwan under grant numbers MOST-110-2221-E-011-038-MY3 and MOST 110-2221-E-011-100-MY3. Dr. Noto Susanto Gultom acknowledged the postdoctoral funding from NSTC under grant number MOST-110-2811-E-011-507. The authors acknowledge Ms. Ju-Hung Ho, who operates X-ray Photoelectron Spectroscopy (XPS, ULVAC-PHI. Inc. / PHI 5000 VersaProbe III) at the Precious Instrumentation Center of the National Taiwan University of Science and Technology.

Appendix A. Supporting information

Supplementary data associated with this article can be found in the online version at doi:10.1016/j.apcatb.2024.124100.

References

- [1] H. Ishaq, I. Dincer, C. Crawford, A review on hydrogen production and utilization: Challenges and opportunities, *Int. J. Hydrog. Energy* 47 (2022) 26238–26264, <https://doi.org/10.1016/j.ijhydene.2021.11.149>.
- [2] C. Wei, R.R. Rao, J. Peng, B. Huang, I.E.L. Stephens, M. Risch, Z.J. Xu, Y. Shao-Horn, Recommended Practices and Benchmark Activity for Hydrogen and Oxygen Electrocatalysis in Water Splitting and Fuel Cells, *Adv. Mater.* 31 (2019) 1806296, <https://doi.org/10.1002/adma.201806296>.
- [3] H.L.S. Santos, P.G. Corradini, M. Medina, J.A. Dias, L.H. Mascaro, NiMo-NiCu Inexpensive Composite with High Activity for Hydrogen Evolution Reaction, *ACS Appl. Mater. Interfaces* 12 (2020) 17492–17501, <https://doi.org/10.1021/acsami.0c00262>.

- [4] T. Zhang, M.Y. Wu, D.Y. Yan, J. Mao, H. Liu, W.B. Hu, X.W. Du, T. Ling, S.Z. Qiao, Engineering oxygen vacancy on NiO nanorod arrays for alkaline hydrogen evolution, *Nano Energy* 43 (2018) 103–109, <https://doi.org/10.1016/j.nanoen.2017.11.015>.
- [5] S.H. Yu, D.H.C. Chua, Toward High-Performance and Low-Cost Hydrogen Evolution Reaction Electrocatalysts: Nanostructuring Cobalt Phosphide (CoP) Particles on Carbon Fiber Paper, *ACS Appl. Mater. Interfaces* 10 (2018) 14777–14785, <https://doi.org/10.1021/acsami.8b02755>.
- [6] M. Kajbafvala, O. Moradlou, A.Z. Moshfegh, CVD growth of the nanostructured Ni₃S₂ thin films as efficient electrocatalyst for hydrogen evolution reaction, *Vacuum* 188 (2021) 110209, <https://doi.org/10.1016/j.vacuum.2021.110209>.
- [7] Y. Lu, Z. Li, Y. Xu, L. Tang, S. Xu, D. Li, J. Zhu, D. Jiang, Bimetallic Co-Mo nitride nanosheet arrays as high-performance bifunctional electrocatalysts for overall water splitting, *Chem. Eng. J.* 411 (2021) 128433, <https://doi.org/10.1016/j.cej.2021.128433>.
- [8] D.H. Kuo, H. Abdullah, N.S. Gultom, J.Y. Hu, Ag-Decorated MoS_x Laminar-Film Electrocatalyst Made with Simple and Scalable Magnetron Sputtering Technique for Hydrogen Evolution: A Defect Model to Explain the Enhanced Electron Transport, *ACS Appl. Mater. Interfaces* 12 (2020) 35011–35021, <https://doi.org/10.1021/acsami.0c09358>.
- [9] N.S. Gultom, D.H. Kuo, H. Abdullah, C.N. Hsu, Fabrication of an Ag₂S-MoS_x/MoNiAg film electrode for efficient electrocatalytic hydrogen evolution in alkaline solution, *Mater. Today Energy* 21 (2021) 100768, <https://doi.org/10.1016/j.mtener.2021.100768>.
- [10] J. Wei, M. Zhou, A. Long, Y. Xue, H. Liao, C. Wei, Z.J. Xu, Heterostructured Electrocatalysts for Hydrogen Evolution Reaction Under Alkaline Conditions, *Nano-Micro Lett.* 10 (2018) 75, <https://doi.org/10.1007/s40820-018-0229-x>.
- [11] Y. Wu, G.-D. Li, Y. Liu, L. Yang, X. Lian, T. Asefa, X. Zou, Overall Water Splitting Catalyzed Efficiently by an Ultrathin Nanosheet-Built, Hollow Ni₃S₂-Based Electrocatalyst, *Adv. Funct. Mater.* 26 (2016) 4839–4847, <https://doi.org/10.1002/adfm.201601315>.
- [12] T. Kou, T. Smart, B. Yao, I. Chen, D. Thota, Y. Ping, Y. Li, Theoretical and Experimental Insight into the Effect of Nitrogen Doping on Hydrogen Evolution Activity of Ni₃S₂ in Alkaline Medium, *Adv. Energy Mater.* 8 (2018) 1703538, <https://doi.org/10.1002/aenm.201703538>.
- [13] L. Tie, N. Li, C. Yu, Y. Liu, S. Yang, H. Chen, S. Dong, J. Sun, S. Dou, J. Sun, Self-Supported Nonprecious MXene/Ni₃S₂ Electrocatalysts for Efficient Hydrogen Generation in Alkaline Media, *ACS Appl. Energy Mater.* 2 (2019) 6931–6938, <https://doi.org/10.1021/acsami.9b01529>.
- [14] N.S. Gultom, C.H. Li, D.H. Kuo, H. Abdullah, Single-Step Synthesis of Fe-Doped Ni₃S₂/FeS₂ Nanocomposites for Highly Efficient Oxygen Evolution Reaction, *ACS Appl. Mater. Interfaces* 14 (2022) 39917–39926, <https://doi.org/10.1021/acsami.2c08246>.
- [15] N.S. Gultom, H. Abdullah, C.N. Hsu, D.H. Kuo, Activating nickel iron layer double hydroxide for alkaline hydrogen evolution reaction and overall water splitting by electrodepositing nickel hydroxide, *Chem. Eng. J.* 419 (2021) 129608, <https://doi.org/10.1016/j.cej.2021.129608>.
- [16] K. Murase, H. Ando, E. Matsubara, T. Hirato, Y. Awakura, Determination of Mo(VI) Species and Composition in Ni-Mo Alloy Plating Baths by Raman Spectra Factor Analysis, *J. Electrochem. Soc.* 147 (2000) 2210, <https://doi.org/10.1149/1.1393509>.
- [17] T.-F. Hung, Z.-W. Yin, S.B. Betzler, W. Zheng, J. Yang, H. Zheng, Nickel sulfide nanostructures prepared by laser irradiation for efficient electrocatalytic hydrogen evolution reaction and supercapacitors, *Chem. Eng. J.* 367 (2019) 115–122, <https://doi.org/10.1016/j.cej.2019.02.136>.
- [18] L. Deng, W. Jia, W. Zheng, H. Liu, D. Jiang, Z. Li, Y. Tian, W. Zhang, J. Liu, Hierarchically magnetic Ni–Al binary layered double hydroxides: towards tunable dual electro/magneto-stimuli performances, *J. Ind. Eng. Chem.* 58 (2018) 163–171, <https://doi.org/10.1016/j.jiec.2017.09.021>.
- [19] C. Wang, H. Shang, Y. Wang, H. Xu, J. Li, Y. Du, Interfacial electronic structure modulation enables CoMoOx/CoOx/RuOx to boost advanced oxygen evolution electrocatalysis, *J. Mater. Chem. A* 9 (2021) 14601–14606, <https://doi.org/10.1039/D1TA01226F>.
- [20] B. Zhu, Q. Hu, X. Liu, G. Li, L. Fan, Q. Zhang, J. Liu, C. He, Boosting the electrochemical water oxidation reaction of hierarchical nanoarrays through NiFe-oxides/Ag heterointerfaces, *Chem. Commun.* 54 (2018) 10187–10190, <https://doi.org/10.1039/C8CC06270F>.
- [21] A. Sun, H. Zhao, M. Wang, J. Ma, H. Jin, K. Zhang, One-Pot Synthesis of Pyrite Nanoplates Supported on Chitosan Hydrochar as Fenton Catalysts for Organics Removal from Water, *Catalysts* 12 (2022) 858, <https://doi.org/10.3390/catal12080858>.
- [22] M. Hou, X. Teng, J. Wang, Y. Liu, L. Guo, L. Ji, C. Cheng, Z. Chen, Multiscale porous molybdenum phosphide of honeycomb structure for highly efficient hydrogen evolution, *Nanoscale* 10 (2018) 14594–14599, <https://doi.org/10.1039/C8NR04246B>.
- [23] H. Li, H. Li, Y. Qiu, S. Liu, J. Fan, X. Guo, Improving oxygen vacancies by cobalt doping in MoO₂ nanorods for efficient electrocatalytic hydrogen evolution reaction, *Nano Sel.* 2 (2021) 2148–2158, <https://doi.org/10.1002/nano.202100075>.
- [24] M. Guo, A. Qayum, S. Dong, X. Jiao, D. Chen, T. Wang, In situ conversion of metal (Ni, Co or Fe) foams into metal sulfide (Ni₃S₂, Co₃S₂ or FeS) foams with surface grown N-doped carbon nanotube arrays as efficient superhydrophobic electrocatalysts for overall water splitting, *J. Mater. Chem. A* 8 (2020) 9239–9247, <https://doi.org/10.1039/D0TA02337J>.
- [25] Y. Zheng, L. He, X. Kong, Y. Song, Y. Zhao, Three-dimensional porous N-doped graphite carbon with embedded CoS₂ nanoparticles as advanced anode for sodium-ion batteries, *Appl. Surf. Sci.* 603 (2022) 154481, <https://doi.org/10.1016/j.apsusc.2022.154481>.
- [26] H. Abdullah, N.S. Gultom, D.-H. Kuo, A simple one-pot synthesis of a Zn(O,S)/Ga₂O₃ nanocomposite photocatalyst for hydrogen production and 4-nitrophenol reduction, *N. J. Chem.* 41 (2017) 12397–12406, <https://doi.org/10.1039/C7NJ02505J>.
- [27] N.S. Gultom, M.Z. Silitonga, D.-H. Kuo, Bimetallic Cobalt–Nickel Electrode Made by a Sputtering Technique for Electrocatalytic Hydrogen Evolution Reaction: Effect of Nickel Ratios, *ACS Appl. Energy Mater.* (2022), <https://doi.org/10.1021/acsami.2c01177>.
- [28] M.Z.S. Noto Susanto Gultom, Kai-Xiang Hu, Yi-Cheng Zhou, Dong-Hau Kuo, Electrodeposition of bimetal Ni-Co oxide as a bifunctional electrocatalyst for rechargeable zinc air battery, *J. Alloy. Compd.* 955 (2023) 170232, <https://doi.org/10.1016/j.jallcom.2023.170232>.
- [29] N.S. Gultom, T.-S. Chen, M.Z. Silitonga, D.-H. Kuo, Overall water splitting realized by overall sputtering thin-film technology for a bifunctional MoNiFe electrode: A green technology for green hydrogen, *Appl. Catal. B: Environ.* 322 (2023) 122103, <https://doi.org/10.1016/j.apcatb.2022.122103>.
- [30] X. Zheng, X. Han, Y. Zhang, J. Wang, C. Zhong, Y. Deng, W. Hu, Controllable synthesis of nickel sulfide nanocatalysts and their phase-dependent performance for overall water splitting, *Nanoscale* 11 (2019) 5646–5654, <https://doi.org/10.1039/C8NR09902B>.
- [31] D. Zhang, L. Jiang, Y. Liu, L. Qiu, J. Zhang, D. Yuan, Ni₃S₂-MoS_x nanorods grown on Ni foam as high-efficient electrocatalysts for overall water splitting, *Int. J. Hydrog. Energy* 44 (2019) 17900–17908, <https://doi.org/10.1016/j.ijhydene.2019.05.157>.
- [32] Y. Yao, J. He, L. Ma, J. Wang, L. Peng, X. Zhu, K. Li, M. Qu, Self-supported Co₉S₈-Ni₃S₂-CNTs/NF electrode with superwetting multistage micro-nano structure for efficient bifunctional overall water splitting, *J. Colloid Interface Sci.* 616 (2022) 287–297, <https://doi.org/10.1016/j.jcis.2022.02.071>.
- [33] Y. Yang, H. Yao, Z. Yu, S.M. Islam, H. He, M. Yuan, Y. Yue, K. Xu, W. Hao, G. Sun, H. Li, S. Ma, P. Zapol, M.G. Kanatzidis, Hierarchical Nanoassembly of MoS₂/Co₉S₈/Ni₃S₂/Ni as a Highly Efficient Electrocatalyst for Overall Water Splitting in a Wide pH Range, *J. Am. Chem. Soc.* 141 (2019) 10417–10430, <https://doi.org/10.1021/jacs.9b04492>.
- [34] Y. Li, X. Wu, J. Wang, H. Wei, S. Zhang, S. Zhu, Z. Li, S. Wu, H. Jiang, Y. Liang, Sandwich structured Ni₃S₂-MoS₂-Ni₃S₂@Ni foam electrode as a stable bifunctional electrocatalyst for highly sustained overall seawater splitting, *Electrochim. Acta* 390 (2021) 138833, <https://doi.org/10.1016/j.electacta.2021.138833>.
- [35] Y. Wu, J. Yin, W. Jiang, H. Li, C. Liu, G. Che, Constructing urchin-like Ni₃S₂@Ni₃B on Ni plate as a highly efficient bifunctional electrocatalyst for water splitting reaction, *Nanoscale* 13 (2021) 17953–17960, <https://doi.org/10.1021/acsami.8b09361>.
- [36] L. Wang, X. Xue, Q. Luan, J. Guo, L. Chu, Z. Wang, B. Li, M. Yang, G. Wang, Interface engineering of Mo-doped Ni₃S₈/Ni₃S₂ multiphase heterostructure nanoflowers by one step synthesis for efficient overall water splitting, *J. Colloid Interface Sci.* 634 (2023) 563–574, <https://doi.org/10.1016/j.jcis.2022.12.064>.
- [37] J. Xu, J. Rong, Y. Zheng, Y. Zhu, K. Mao, Z. Jing, T. Zhang, D. Yang, F. Qiu, Construction of sheet-on-sheet hierarchical MoS₂/NiS₂ heterostructures as efficient bifunctional electrocatalysts for overall water splitting, *Electrochim. Acta* 385 (2021) 138438, <https://doi.org/10.1016/j.electacta.2021.138438>.
- [38] Q. Wu, A. Dong, C. Yang, L. Ye, L. Zhao, Q. Jiang, Metal-organic framework derived Co₃O₄@Mo-Co₃S₄-Ni₃S₂ heterostructure supported on Ni foam for overall water splitting, *Chem. Eng. J.* 413 (2021) 127482, <https://doi.org/10.1016/j.cej.2020.127482>.
- [39] Y. Wu, Y. Li, M. Yuan, H. Hao, X. San, Z. Lv, L. Xu, B. Wei, Operando capturing of surface self-reconstruction of Ni₃S₂/FeNi₃S₄ hybrid nanosheet array for overall water splitting, *Chem. Eng. J.* 427 (2022) 131944, <https://doi.org/10.1016/j.cej.2021.131944>.
- [40] W. Yaseen, M. Xie, B.A. Yusuf, Y. Xu, M. Rafiq, N. Ullah, P. Zhou, X. Li, J. Xie, Hierarchical Co/MoO₂@N-doped carbon nanosheets derived from waste lotus leaves for electrocatalytic water splitting, *Int. J. Hydrog. Energy* 47 (2022) 15673–15686, <https://doi.org/10.1016/j.ijhydene.2022.03.037>.
- [41] Y. Lv, M. Chen, N. Suo, X. He, L. Cui, The construction of highly active bifunctional electrocatalyst of VS₄/Ni₃S₂ heterostructure for electrochemical water splitting, *J. Electroanal. Chem.* 927 (2022) 116979, <https://doi.org/10.1016/j.jelechem.2022.116979>.
- [42] Z. Sun, X. Wang, M. Yuan, H. Yang, Y. Su, K. Shi, C. Nan, H. Li, G. Sun, J. Zhu, X. Yang, S. Chen, Lewis Base-Hungry” Amorphous–Crystalline Nickel Borate–Nickel Sulfide Heterostructures by In Situ Structural Engineering as Effective Bifunctional Electrocatalysts toward Overall Water Splitting, *ACS Appl. Mater. Interfaces* 12 (2020) 23896–23903, <https://doi.org/10.1021/acsami.0c03796>.
- [43] Y. Zheng, L. Wang, J. Pang, K. Sun, J. Hou, G. Wang, W. Guo, L. Chen, Ni₃S₂/Co₉S₈ embedded poor crystallinity NiCo layered double hydroxides hierarchical nanostructures for efficient overall water splitting, *J. Colloid Interface Sci.* 637 (2023) 85–93, <https://doi.org/10.1016/j.jcis.2023.01.074>.
- [44] Q.-N. Ha, N. Susanto Gultom, C.-H. Yeh, D.-H. Kuo, One-pot synthesized Li, V co-doped Ni₃S₂ nanorod arrays as a bifunctional electrocatalyst for industrialization-facile hydrogen production via alkaline exchange membrane water electrolysis, *Chem. Eng. J.* 472 (2023) 144931, <https://doi.org/10.1016/j.cej.2023.144931>.
- [45] J. Fang, X. Qian, J. Xia, B. Huang, G. He, Z. Zhang, H. Chen, Heterostructure engineering of self-supported bimetallic sulfide as an efficient bifunctional electrocatalyst for overall water splitting, *J. Alloy. Compd.* 937 (2023) 168339, <https://doi.org/10.1016/j.jallcom.2022.168339>.

- [46] Q. Li, W. Zhang, J. Shen, X. Zhang, Z. Liu, J. Liu, Trimetallic nanoplate arrays of Ni-Fe-Mo sulfide on FeNi₃ foam: A highly efficient and bifunctional electrocatalyst for overall water splitting, *J. Alloy. Compd.* 902 (2022) 163670, <https://doi.org/10.1016/j.jallcom.2022.163670>.
- [47] H. Xie, Y. Feng, X. He, Y. Zhu, Z. Li, H. Liu, S. Zeng, Q. Qian, G. Zhang, Construction of Nitrogen-Doped Biphasic Transition-Metal Sulfide Nanosheet Electrode for Energy-Efficient Hydrogen Production via Urea Electrolysis, *Small* 19 (2023) 2207425, <https://doi.org/10.1002/smll.202207425>.
- [48] N. Li, S. Qu, J. Ma, W. Shen, Core-shell-structured CoS₂@N-doped carbon nanoneedle array as an efficient bifunctional electrocatalyst for overall water splitting, *Int. J. Hydrog. Energy* 48 (2023) 180–195, <https://doi.org/10.1016/j.ijhydene.2022.09.217>.
- [49] P. Li, L. Zhang, Y. Yao, T. Xie, W. Du, T. Zhao, J. Jiang, ZnCoNiS nanoflowers electrodes with rich heterointerface as efficient bifunctional electrocatalyst for overall water splitting, *Int. J. Hydrog. Energy* (2023), <https://doi.org/10.1016/j.ijhydene.2023.07.353>.
- [50] C. Feng, M. Chen, Y. Zhou, Z. Xie, X. Li, P. Xiaokaiti, Y. Kansha, A. Abudula, G. Guan, High-entropy NiFeCoV disulfides for enhanced alkaline water/seawater electrolysis, *J. Colloid Interface Sci.* 645 (2023) 724–734, <https://doi.org/10.1016/j.jcis.2023.04.172>.
- [51] B. Chong, M. Xia, Y. Lv, H. Li, X. Yan, B. Lin, G. Yang, Hierarchical phosphorus-oxygen incorporated cobalt sulfide hollow micro/nano-reactor for highly-efficient electrocatalytic overall water splitting, *Chem. Eng. J.* 465 (2023) 142853, <https://doi.org/10.1016/j.cej.2023.142853>.
- [52] M. Kumar, T.C. Nagaiah, A NiCu–MoS₂ electrocatalyst for pH-universal hydrogen evolution reaction and Zn–air batteries driven self-power water splitting, *J. Mater. Chem. A* 11 (2023) 18336–18348, <https://doi.org/10.1039/D3TA02668J>.
- [53] Z. Chen, X. Duan, W. Wei, S. Wang, B.-J. Ni, Recent advances in transition metal-based electrocatalysts for alkaline hydrogen evolution, *J. Mater. Chem. A* 7 (2019) 14971–15005, <https://doi.org/10.1039/C9TA03220G>.
- [54] N.S. Gultom, H. Abdullah, J.C. Xie, H. Shuwanto, D.H. Kuo, Improved Hydrogen Production Rate of a Nickel-Doped Zinc Indium Oxysulfide Visible-Light Catalyst: Comparative Study of Stoichiometric and Nonstoichiometric Compounds, *Acs Appl. Energy Mater.* 5 (2022) 1755–1766, <https://doi.org/10.1021/acsaem.1c03200>.
- [55] N.T. Suen, S.F. Hung, Q. Quan, N. Zhang, Y.J. Xu, H.M. Chen, Electrocatalysis for the oxygen evolution reaction: recent development and future perspectives, *Chem. Soc. Rev.* 46 (2017) 337–365, <https://doi.org/10.1039/C6CS00328A>.